

Profile Bayesian Optimization for Expensive Computer Experiments

Courtney Kyger ^{*} James Fernandez [†] John A. Grunenwald [†] James Braun [†]
 Annie S. Booth [‡]

December 30, 2025

Abstract

We propose a novel Bayesian optimization (BO) procedure aimed at identifying the “profile optima” of a deterministic black-box computer simulation that has a single control parameter and multiple nuisance parameters. The profile optima capture the optimal response values as a function of the control parameter. Our objective is to identify them across the entire plausible range of the control parameter. Classic BO, which targets a single optimum over all parameters, does not explore the entire control parameter range. Instead, we develop a novel two-stage acquisition scheme to balance exploration across the control parameter and exploitation of the profile optima, leveraging deep and shallow Gaussian process surrogates to facilitate uncertainty quantification. We are motivated by a computer simulation of a diffuser in a rotating detonation combustion engine, which returns the energy lost through diffusion as a function of various design parameters. We aim to identify the lowest possible energy loss as a function of the diffuser’s length; understanding this relationship will enable well-informed design choices. Our “profile Bayesian optimization” procedure outperforms traditional BO and profile optimization methods on a variety of benchmarks and proves effective in our motivating application.

Keywords: expected improvement, Gaussian process, deep Gaussian process, surrogate, triangulation candidates, uncertainty quantification

1 Introduction

Computer simulations (or “computer experiments”) are becoming increasingly relevant in physical and engineering sciences, where they may supplement physical experimentation that is costly, dangerous, or infeasible. In this work we tackle profile optimization of black-box computer simulations, seeking the optimal response value over the full support of a specified “control parameter.” Profile optimization can provide crucial information about trade-offs between performance and an important parameter, thereby supporting informed decision making.

Let $f : \mathcal{X} \rightarrow \mathbb{R}$ denote a black-box simulation that accepts d -dimensional input $\mathbf{x} \in \mathcal{X} \subset \mathbb{R}^d$ and returns scalar $y = f(\mathbf{x})$. Inputs are further delineated into a single control parameter $x^* \in \mathcal{X}^* \subset \mathbb{R}$ and nuisance parameters $\mathbf{x}^{-*} \in \mathcal{X}^{-*} \subset \mathbb{R}^{d-1}$ such that $\mathbf{x} = [x^*, \mathbf{x}^{-*}]$, $\mathcal{X} = \{\mathcal{X}^*, \mathcal{X}^{-*}\}$, and $f(\mathbf{x}) = f(x^*, \mathbf{x}^{-*})$. For a given control parameter, the profile optima of f is defined as

$$T(x^*) := \min_{\mathbf{x}^{-*} \in \mathcal{X}^{-*}} f(x^*, \mathbf{x}^{-*}) \quad \forall x^* \in \mathcal{X}^*, \quad (1)$$

^{*}Corresponding Author: Department of Statistics, Virginia Tech, ston2874@vt.edu

[†]Department of Mechanical and Aerospace Engineering, NC State University

[‡]Department of Statistics, Virginia Tech

providing the minimum response that can be obtained for any value of the control parameter. To visualize this in a simple setting, Figure 1 portrays the two-dimensional Branin function (Surjanovic and Bingham, 2013) scaled to $\mathcal{X} = [0, 1]^2$ with the resulting $T(x^*)$.

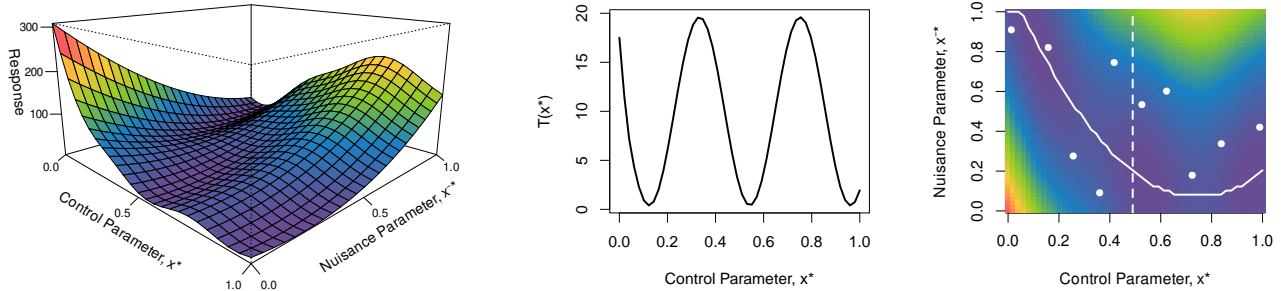


Figure 1: Branin function with one control parameter and one nuisance parameter (left), with the true $T(x^*)$ (center). Right panel shows the location of $T(x^*)$ in \mathcal{X} (solid white), an LHS design of size $n = 10$ (white circles), and the vertical slice that features later in Figure 2 (dashed white).

Our real-world motivation stems from the design of a jet engine: a rotating detonation combustor (RDC) that pushes hot air through a diffuser to power a gas turbine. Computational fluid dynamics simulations compute the flow through the diffuser, estimating the energy lost through diffusion as a function of the design parameters (i.e., curvature, bypass locations, and diffuser length). The longest diffuser length will result in the smallest energy loss regardless of the remaining parameter values, but shorter diffusers are more cost-effective and practical. Our objective is to estimate the profile optima in energy loss as a function of diffuser length to facilitate effective decision-making concerning the diffuser’s design. The key challenge in estimating $T(x^*)$ is the computational expense of evaluating the computer simulation. Simplified versions of our RDC simulation require 10 minutes of computation to produce a single observation, even with high performance parallel computing. Higher fidelity versions may require several hours.

When simulation data is limited, as in our motivating application, a surrogate model is essential. Surrogates are trained on observations of the simulator in order to provide predictions and uncertainty quantification (UQ) at unobserved inputs. Gaussian process (GP) surrogates are the “go-to” choice (Santner et al., 2003; Rasmussen and Williams, 2006; Gramacy, 2020), but in their canonical form they may be too rigid to accommodate the complexity of modern computer simulations for physical systems. Deep Gaussian processes (DGPs; Damianou and Lawrence, 2013) offer increased flexibility by warping the input space through latent Gaussian layers and have been gaining significant attention as surrogates for non-stationary simulations (e.g., Rajaram et al., 2021; Marmin and Filippone, 2022; Sauer, 2023; Yazdi et al., 2024). Crucially, our contribution is suitable for both GP and DGP surrogates.

Direct optimization of expensive computer experiments, i.e., $\min_{\mathbf{x} \in \mathcal{X}} f(\mathbf{x})$, is a well studied problem, usually tackled through Bayesian optimization (BO; Frazier, 2018; Pourmohamad and Lee, 2021; Wang et al., 2023). BO involves a greedy feedback loop where design points are sequentially selected based on information from a surrogate model that has been trained on the previously observed data and is updated after each new acquisition. Common acquisition strategies include maximization of expected improvement (EI; Jones et al., 1998; Zhan and Xing, 2020) and Thompson sampling (Thompson, 1933). Naturally, BO methods that target the global optimum are ill-equipped for profile optimization as they are not designed to explore the entire control parameter space.

Ginsbourger et al. (2014) proposed “profile expected improvement” (PEI) to remedy this disconnect. PEI modifies traditional EI in order to target the profile optima instead of the global optimum, but it has its own challenges. Acquisitions based on PEI, as proposed by Ginsbourger et al., are computationally expensive to obtain as the requisite computations are incompatible with numerical optimizers. We suspect this is the reason they only provided results on two-dimensional problems. Even when we adapt the implementation to facilitate faster acquisitions (more on this in Section 3), PEI tends to over-exploit and under-explore, resulting in acquisitions clustered near the global optimum. The tendency to under-explore is a well-known limitation of traditional EI (Qin et al., 2017; Berk et al., 2018; Chen et al., 2024), and our simulations (Section 4) show that PEI tends to inherit this same fate.

We propose a novel profile Bayesian optimization (PBO) procedure to effectively estimate $T(x^*)$ with limited observations of the black-box function $f(\mathbf{x})$. We leverage joint posterior draws from a Bayesian GP or DGP surrogate to estimate $T(x^*)$ with thorough uncertainty quantification. We select the next acquisition, \mathbf{x}_{n+1} , in two stages: first, choosing x_{n+1}^* based on exploration of \mathcal{X}^* , then choosing \mathbf{x}_{n+1}^{-*} based on exploitation of $T(x_{n+1}^*)$ through optimization of PEI along the x_{n+1}^* slice. The intentional exploration of the first step provides effective coverage of the control parameter space, while the exploitation of the second step hones in on the profile optima. We also propose a strategic adaptation of triangulation candidates (“tricands”; Gramacy et al., 2022) to alleviate computational bottlenecks in our procedure.

The remainder of this paper is organized as follows. Section 2 reviews the essential building blocks of our method. Section 3 details our PBO procedure. Section 4 provides a variety of synthetic examples to validate our approach against state-of-the-art alternatives. Finally, we present the results of our method on the RDC in Section 5 and conclude in Section 6.

2 Building Blocks

In this section, we detail some of the building blocks that are necessary for our contribution, including GP and DGP surrogates, traditional expected improvement, and profile expected improvement. Throughout, we use lowercase letters to represent scalars, bold lowercase letters to represent vectors, and bold uppercase letters to represent matrices. Specifically, let \mathbf{X} denote a matrix of row-stacked inputs with response $\mathbf{y} = f(\mathbf{X})$. In all exercises, we prescale inputs to the unit hypercube ($\mathcal{X} = [0, 1]^d$) and prescale responses to zero mean with unit variance before fitting our surrogates.

2.1 GP and DGP Surrogates

A Gaussian process prior assumes responses were generated as a realization of a random Gaussian process such that any finite set of observations is distributed as a multivariate normal distribution, e.g., $\mathbf{y} \sim \mathcal{N}(\boldsymbol{\mu}, K(\mathbf{X}))$. We set $\boldsymbol{\mu} = \mathbf{0}$ after centering responses. We define the covariance matrix $K(\mathbf{X})$ with elements $K(\mathbf{X})^{(ij)} = \tau^2 (k(\|\mathbf{x}_i - \mathbf{x}_j\|^2) + g\mathbb{I}_{i=j})$, where kernel $k(\cdot)$ returns the correlation between y_i and y_j as a function of the Euclidean distance between their inputs, \mathbf{x}_i and \mathbf{x}_j . For our deterministic computer simulations, we fix $g = 1 \times 10^{-6}$ to preserve interpolation while providing numerical stability. Scale parameter τ^2 and any other hyperparameters within the kernel may be inferred through maximum likelihood estimation or sampled in a Bayesian framework.

Conditioned on n observations, $\mathcal{D}_n = \{\mathbf{X}_n, \mathbf{y}_n\}$, the posterior distribution of f is itself a Gaussian process. When restricted to a finite set of locations \mathbf{X}_p of size $n_p \times d$, the posterior is expressed as

$$f_n(\mathbf{X}_p) \mid \mathcal{D}_n \sim \mathcal{N}_{n_p}(\mu_n(\mathbf{X}_p), \Sigma_n(\mathbf{X}_p)) \quad \text{where} \quad \begin{aligned} \mu_n(\mathbf{X}_p) &= K(\mathbf{X}_p, \mathbf{X}_n)K(\mathbf{X}_n)^{-1}\mathbf{y}_n \\ \Sigma_n(\mathbf{X}_p) &= K(\mathbf{X}_p) - K(\mathbf{X}_p, \mathbf{X}_n)K(\mathbf{X}_n)^{-1}K(\mathbf{X}_n, \mathbf{X}_p). \end{aligned} \quad (2)$$

Here, $K(\mathbf{X}_p, \mathbf{X}_n)$ denotes the $n_p \times n$ matrix of covariances between each row of \mathbf{X}_p and each row of \mathbf{X}_n . To demonstrate, we trained a GP surrogate for the Branin function using a random Latin hypercube sample (LHS; McKay et al., 2000) of size $n = 10$ (indicated by the white circles in Figure 1). The left panel of Figure 2 shows $\mu_{10}(\mathbf{X}_p)$ (solid blue) and its 95% credible interval (dashed blue) along the slice $x^* = 0.48$, where \mathbf{X}_p contains a fine and evenly-spaced grid of x^{-*} values in one dimension. The GP offers nonlinear predictions with effective UQ. Posterior uncertainty is lower near the training data—a GP hallmark.

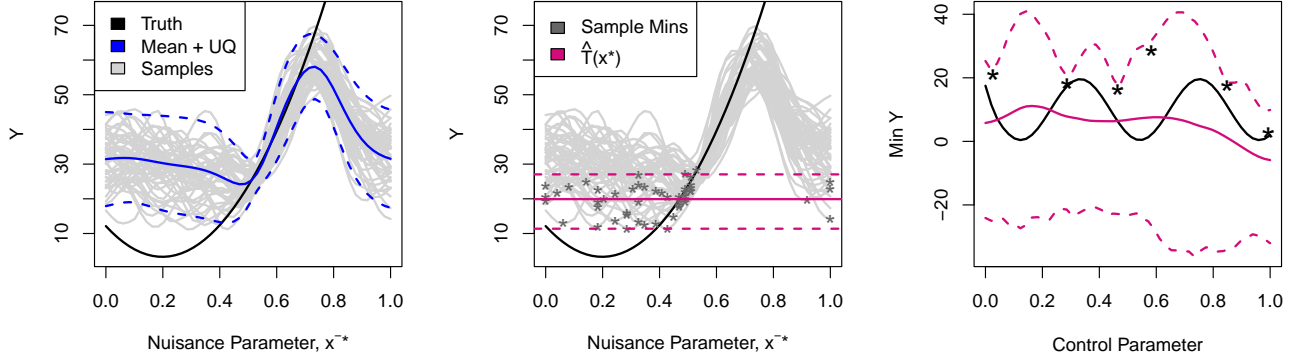


Figure 2: *Left:* GP trained on a random LHS of size $n = 10$ (white circles in Figure 1) for the 2D Branin function, shown along the slice $x^* = 0.48$ with the posterior mean and 95% CI in blue. Gray lines show 50 samples from this posterior. *Center:* The minimum values of each posterior sample (dark gray stars). Dark pink lines mark the the mean and 95% quantiles of 1,000 such minimums. *Right:* Estimation of the full $\hat{T}(x^*)$ (dark pink) with the truth in solid black. Black stars mark observed (x_i^*, y_i) for $i = 1, \dots, n$ (some observations are cut off above).

Joint posterior samples may be obtained by sampling realizations from this multivariate normal distribution, such as those shown in gray in Figure 2. The granularity of these joint samples depends on the density of the predictive locations, \mathbf{X}_p . A fine grid, while sufficient in one dimension, becomes too cumbersome in higher dimensions. Even though the computation of $\mu_n(\mathbf{X}_p)$ and $\Sigma_n(\mathbf{X}_p)$ in Eq. (2) is at most quadratic in n_p , drawing joint samples from $f_n(\mathbf{X}_p)$ requires decomposition of $\Sigma_n(\mathbf{X}_p)$, which is cubic in n_p . To avoid this bottleneck, it is common to stick with point-wise predictions, treating each row of \mathbf{X}_p independently. But when joint posterior samples are necessary (as in our proposed framework), Vecchia approximation (Vecchia, 1988) can offer some reprieve. Vecchia-approximated joint posterior samples are obtained by sequentially drawing observations from the univariate Gaussian posterior distribution of each predictive location, while allowing these posteriors to condition on previously sampled values. Moving forward, we will use Vecchia approximation for faster posterior sampling; see Katzfuss et al. (2020) and Katzfuss and Guinness (2021) for further details on Vecchia-approximated GPs.

While GPs offer flexible nonlinear regression, they are limited by the stationarity of the covariance kernel. The GP covariance structure is based solely on the Euclidean distance between inputs, which can be a severe handicap for response surfaces with regime shifts or starkly varying dynamics (Booth et al., 2024). Deep Gaussian processes (Damianou and Lawrence, 2013) upgrade typical GPs through functional compositions, providing additional flexibility to accommodate complex nonstationary functions. Latent Gaussian layers serve as spatial deformations of the input space (Sampson and Guttorp, 1992; Schmidt and O'Hagan, 2003). While they may vary in width and depth, the most common structure for DGP surrogates contains one latent layer with conditionally independent “nodes” of dimension d (Sauer et al., 2023c). Specifically,

$$\begin{aligned} \mathbf{y} &\sim \mathcal{N}(\boldsymbol{\mu}_y, K(\mathbf{W})) & \text{for } i = 1, \dots, d & \text{ where } \mathbf{W} = [\mathbf{w}_1 \ \dots \ \mathbf{w}_d]. \\ \mathbf{w}_i &\sim \mathcal{N}(\boldsymbol{\mu}_w, K(\mathbf{X})) \end{aligned} \quad (3)$$

Prior means of $\boldsymbol{\mu}_y = \boldsymbol{\mu}_w = \mathbf{0}$ are common, although setting the prior mean of \mathbf{w}_i to the i^{th} column of \mathbf{X} may provide a helpful degree of regularization. Latent \mathbf{W} is the driver of nonstationary flexibility but can be difficult to infer. Bayesian posterior integration through elliptical slice sampling (ESS; [Murray et al., 2010](#)) has been shown to excel in modeling of complex deterministic computer experiments (e.g., [Sauer et al., 2023a](#); [Ming et al., 2023](#); [Booth et al., 2025](#)). Conditioned on \mathcal{D}_n , ESS provides posterior samples $\mathbf{W}_n^{(t)}$, where t indexes the MCMC iteration. These in turn facilitate inference of warped $\mathbf{W}_p^{(t)}$ for predictive locations \mathbf{X}_p . Ultimately, joint posterior draws of $f_n(\mathbf{X}_p)$ may be obtained through application of Eq. (2) with warped/inferred $\mathbf{W}_n^{(t)}$ and $\mathbf{W}_p^{(t)}$ in place of \mathbf{X}_n and \mathbf{X}_p . See [Sauer et al. \(2023c\)](#) for specifics. Vecchia approximation is also available to enable faster DGP posterior sampling ([Sauer et al., 2023b](#)). While we use traditional GPs for our illustrative examples (Figures 1-3), the nonstationary flexibility of the DGP is essential for our motivating RDC simulation.

With a trained GP or DGP surrogate in-hand, estimation of $T(x^*)$ may proceed as follows. First, generate joint samples from the posterior distribution at $\mathbf{X}_p \in \mathcal{X}$ locations (we will discuss the choice of \mathbf{X}_p in Section 3). Then, save the minimum response value attained in each posterior sample for each unique value of $x^* \in \mathbf{X}_p$. Together, the empirical distribution of these minimums serves as the estimate $\hat{T}(x^*)$. We will summarize this distribution through its mean, denoted $\mu_T(x^*)$, and 95th percentiles, denoted $\text{CI}_T(x^*)$. Grabbing the minimum from a joint posterior sample is reminiscent of Thompson sampling, where the minimum of a single sample is used as the next acquisition in a BO loop.

Figure 2 illustrates this process for the GP trained on 10 observations of the Branin function. We drew 1,000 posterior samples across a dense two-dimensional grid ($\mathbf{X}_p = [0, 0.01, \dots, 0.99, 1] \otimes [0, 0.01, \dots, 0.99, 1]$). The left panel shows 50 of these samples (gray lines) along the slice $x^* = 0.48$. For each sample, we isolate the minimum observed y -value; these are marked by the dark gray stars in the center panel. Although we only show 50 here for demonstration, we use the minimums of all 1,000 samples to generate the mean and 95th percentiles shown in solid/dashed pink. We repeat this process of grabbing and aggregating the minimums along each x^* slice, using the same joint posterior samples (which were drawn over the entire two-dimensional space). Sampling from the posterior over the full d -dimensional space is essential to incorporate the smoothly varying covariance structure across x^* . Together, the mean/percentiles taken along each slice provide an estimate of the complete $T(x^*)$, as shown in the right panel. The large uncertainty in Figure 2 is a byproduct of a small n ; we can reduce uncertainty through sequential acquisitions.

2.2 Expected Improvement

Given a surrogate $f_n(\mathbf{x})$, trained on observed \mathcal{D}_n , Bayesian optimization selects the next input as $\mathbf{x}_{n+1} = \text{argmax}_{\mathbf{x} \in \mathcal{X}} h(\mathbf{x})$ where $h(\mathbf{x})$ is some “acquisition function” that quantifies the utility of a potential acquisition. If the acquisition function has a closed-form and is quick to evaluate, it may be fed through a numerical optimizer, such as a multi-start gradient descent. If evaluation of $h(\mathbf{x})$ is cumbersome, a discrete search over a set of potential candidates is usually preferred. Once selected, $y_{n+1} = f(\mathbf{x}_{n+1})$ is observed, n is incremented, the surrogate is updated, and the process is repeated until a stopping criterion is met or the computation budget is exhausted.

For typical BO, the most common acquisition function is expected improvement ([Jones et al., 1998](#)). For global optimization, a new acquisition would offer improvement if its response value is below the lowest response we have observed thus far (denoted y_{\min}). EI takes the expectation of this improvement, which

has a closed form under a GP surrogate:

$$EI(\mathbf{x} | \mathcal{D}_n) = (\mu_n(\mathbf{x}) - y_{\min}) \Phi \left(\frac{\mu_n(\mathbf{x}) - y_{\min}}{\sigma_n(\mathbf{x})} \right) + \sigma_n(\mathbf{x}) \phi \left(\frac{\mu_n(\mathbf{x}) - y_{\min}}{\sigma_n(\mathbf{x})} \right) \text{ where } y_{\min} = \min(\mathbf{y}_n). \quad (4)$$

Here, $\mu_n(\mathbf{x})$ and $\sigma_n(\mathbf{x}) = \sqrt{\Sigma_n(\mathbf{x})}$ follow Eq. (2), $\Phi(\cdot)$ is the standard normal CDF, and $\phi(\cdot)$ is the standard normal PDF.

To demonstrate, the left panel of Figure 3 shows EI across \mathcal{X} for our running Branin function example. The black circles mark the true global minima (there are three for this function). Notice, one of our random LHS points (white circles) landed very close to a true minimum. The resulting GP surrogate does not think there is improvement to be made elsewhere; the only region of high EI is in the locality of this observed low point. If our goal is to locate a global optimum, this EI surface would lead us right to it. But if our goal is to learn all the profile optima (the entire black line), EI is not an effective acquisition function. It is not designed to explore across the range of the control parameter. As we can see in the right panel of Figure 3, EI is near zero on this slice because y_{\min} is below the posterior samples (the gray lines) generated by our surrogate.

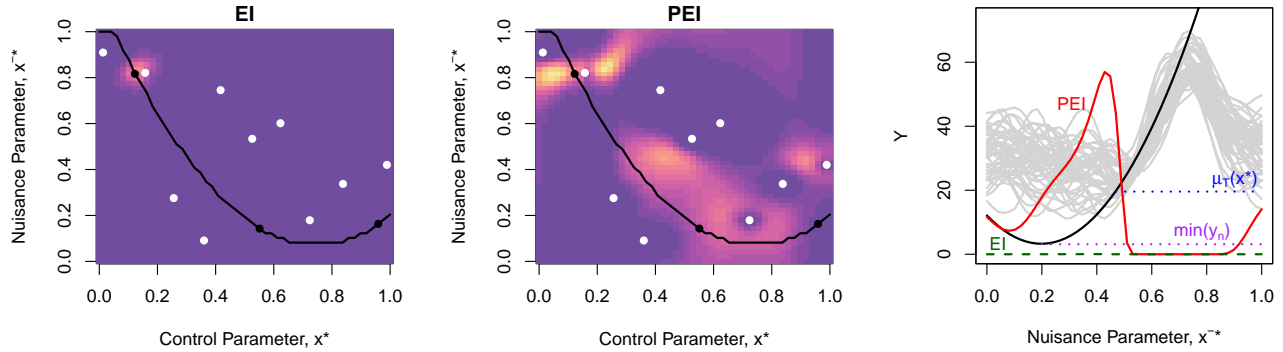


Figure 3: *Left/Center*: EI and PEI (purple/low, yellow/high) for the Branin function. White circles mark training data locations. Black line/circles mark the true profile/global optima. *Right*: The same slice shown in Figure 2, this time with EI (dashed green) and PEI (solid red) overlaid. Horizontal dotted lines mark y_{\min} (purple, used for EI) and estimated $\mu_T(x^*)$ (blue, used for PEI).

2.3 Profile Expected Improvement

In traditional optimization, “improvement” is only achieved if the acquired response value is lower than all previously observed responses, i.e., $f(\mathbf{x}_{n+1}) < y_{\min}$. But in profile optimization, a new acquisition would offer “improvement” if its response is below the previously observed responses *for the same x^* value*. EI is not suited for profile optimization simply because of its use of y_{\min} . The natural solution is to upgrade y_{\min} to a new quantity that acts as a function of x^* , say $t_{\min}(x^*)$. This quantity should capture our existing knowledge about the lowest response value for a particular x^* . Unfortunately, given our limited training data we can not rely on \mathcal{D}_n to provide $t_{\min}(x^*)$ directly. Instead, we need an estimate that can be evaluated for any $x^* \in \mathcal{X}^*$ beyond those that are in \mathcal{D}_n .

Ginsbourger et al. (2014) proposed using the estimated $\mu_T(x^*)$, as described in Section 2.1, in place of y_{\min} in the traditional EI criterion. They also implemented a strategic safeguard to protect against situations where $\mu_T(x^*)$ may be low simply due to high uncertainty. We have already seen that very low y_{\min} values result in flat and uninformative EI surfaces (Figure 3). To avoid this phenomenon with

PEI, [Ginsbourger et al.](#) use the traditional y_{\min} value in areas where it is higher than $\mu_T(x^*)$. Selecting the higher of these values is a conservative approach that avoids over-flattening the acquisition surface. Formally, this “profile expected improvement” criterion is defined as

$$\text{PEI}(\mathbf{x} = \{x^*, \mathbf{x}^{-*}\} \mid \mathcal{D}_n) = (\mu_n(\mathbf{x}) - t_{\min}(x^*)) \Phi \left(\frac{\mu_n(\mathbf{x}) - t_{\min}(x^*)}{\sigma_n(\mathbf{x})} \right) + \sigma_n(\mathbf{x}) \phi \left(\frac{\mu_n(\mathbf{x}) - t_{\min}(x^*)}{\sigma_n(\mathbf{x})} \right) \quad (5)$$

where $t_{\min}(x^*) = \max(y_{\min}, \mu_T(x^*))$.

We offer two visuals of PEI for our running Branin function example. First, the right panel of Figure 3 shows PEI along the slice $x^* = 0.48$. The horizontal dotted blue line marks $\mu_T(x^* = 0.48)$. By using this higher value in place of y_{\min} , PEI is able to offer an informative acquisition surface, targeting the minimum on this slice even though it is higher than the minimum response over the entire domain. As a second visual, the center panel of Figure 3 shows PEI across both dimensions. PEI targets more of the profile optima instead of focusing only on a global optimum.

While PEI is a helpful extension of EI for profile optimization, its calculation is very burdensome. Optimization of PEI first requires estimation of $\mu_T(x^*)$ for any potential x^* . Estimation of $\mu_T(x^*)$ requires potentially thousands of posterior samples at a dense set of predictive locations \mathbf{X}_p . These computations will not integrate nicely in a numerical optimizer. [Ginsbourger et al.](#) employed 50×50 grids in two dimensions but did not expand beyond a single control parameter and a single nuisance parameter. Furthermore, despite its attempts to target all profile optima, PEI tends towards excessive exploitation. Consider the center panel of Figure 3; although there are local optima in the PEI surface across the range of x^* , the global optimum (where \mathbf{x}_{n+1} would be selected), still hovers around the location of y_{\min} . We find that PEI often clusters acquisitions around global optima, struggling to explore the entire \mathcal{X}^* .

3 Profile Bayesian Optimization

Motivated by the drawbacks of PEI as an acquisition function for profile optimization, we propose a new profile Bayesian optimization procedure that involves two crucial upgrades. First, we develop a novel candidate scheme building upon the work of [Gramacy et al. \(2022\)](#) that facilitates efficient posterior sampling for the estimation of $T(x^*)$ and enables acquisitions from smaller candidate sets. Second, we propose a two-stage acquisition method: the first step forces the exploration of $T(x^*)$ across the full support of x^* by choosing the x^* with the largest uncertainty; the second step uses PEI to exploit the best acquisition in \mathcal{X}^{-*} for the chosen x^* .

3.1 Modified Tricands

Estimation of $T(x^*)$ requires joint random samples from the posterior distribution at a discrete number of input locations \mathbf{X}_p . The choice of \mathbf{X}_p can make-or-break this estimation. Although these samples should be drawn over the entire d -dimensional space, consider first a slice along a particular x^* , such as those shown in Figure 2. For each sample (gray line), we grab the minimum response value observed at the \mathbf{X}_p locations along that slice (dark gray stars). If \mathbf{X}_p does not contain the point where the actual minimum is, then we will miss the minimum altogether. In one dimension, we can be pretty confident that a dense evenly spaced grid will include the minimum, but dense grids are infeasible in higher dimensions. Our RDC simulation has 6 inputs—even a semi-dense grid with 50 points per dimension would require upwards of 15 billion points in \mathbf{X}_p .

Instead of grids, we leverage smaller “candidate” sets whose strategic allocation enables their size to be much less than the comparable grid. The number of points in \mathbf{X}_p does not need to be large as long as it

includes the locations where the minimum will be found. We can target these locations using geometric intuition about where extrema are likely to occur. In a GP surrogate, posterior uncertainty inflates as distance from the training data grows—notice $\Sigma_n(\mathbf{X}_p)$ in Eq. (2) is only a function of the Euclidean distances among training and predictive locations. A random sample from the posterior is likely to have its lowest point in one of these regions of highest uncertainty—directly “between” training data locations. In one dimension, these locations include “internal candidates” at the midpoints of each consecutive pair of training locations and “fringe candidates” between the outermost observations and the boundary of \mathcal{X} .

In higher dimensions, the concept of “between” is a little murkier. [Gramacy et al. \(2022\)](#) proposed “tricands” (short for triangulation candidates) for this very purpose. Tricands leverage a Delaunay triangulation of \mathbf{X}_n to allocate candidates between existing training data locations. The triangulation connects observations in \mathbf{X}_n creating non-overlapping triangles/tetrahedra/polychora/etc. depending on dimension. The dashed black lines in the center panel of Figure 4 illustrate the Delaunay triangulation of some \mathbf{X}_n (black circles) in two dimensions.

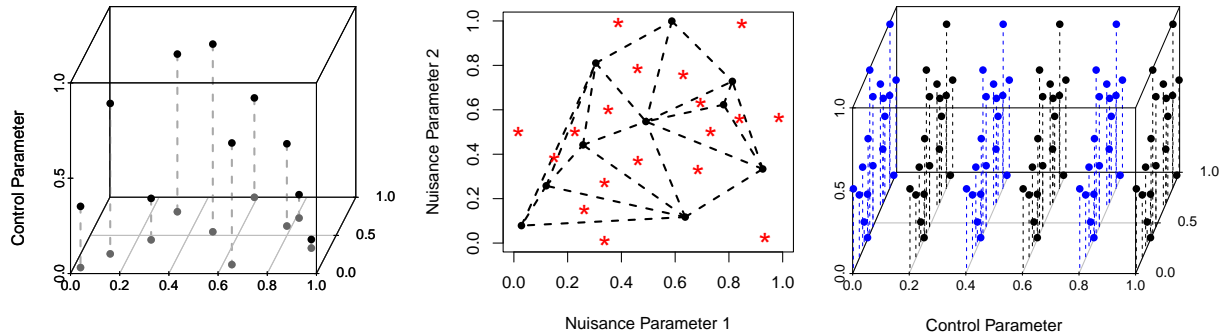


Figure 4: *Left:* Projection of 3D LHS onto 2D nuisance parameter space. *Center:* Tricands (red stars) of 10-point LHS (black points). Dashed black lines represent the Delaunay triangulation. *Right:* Tricands repeated on 6 slices for $x^* \in \{0, 0.2, 0.4, 0.6, 0.8, 1\}$ (colors used for visual clarity).

Tricands are allocated in two groups. Internal candidates are placed at the geometric centers of the triangulation’s components. In Figure 4, these are the red stars inside the triangles. Fringe candidates are placed between the outermost edges and the boundaries of \mathcal{X} . In Figure 4, these are the red stars not contained in any triangle. [Gramacy et al. \(2022\)](#) implemented a tuning parameter controlling how far to set fringe candidates between the triangulation and the border. In our exercises, we allocate fringe candidates at 90% of the distance to the border, since we often find minima live near the boundary. Through this strategic allocation conditioned on \mathbf{X}_n , tricands can cover regions where minima are likely to be sampled with a reasonably small candidate set size.

Tricands provide an efficient set of candidates suitable for finding the minimum of a function. This is appropriate for our nuisance parameters, where the only objective is to find the minimum in \mathcal{X}^{-*} for each x^* . Our objective regarding the control parameter is different: we seek to estimate $T(x^*)$ across the full support of x^* . Tricands does not offer the coverage we need over \mathcal{X}^* , but this coverage can easily be achieved with a semi-dense grid. To fulfill both objectives, we combine a grid over the control parameter with tricands over the nuisance parameters.

We begin by projecting \mathbf{X}_n onto the nuisance space, \mathcal{X}^{-*} , to find \mathbf{X}_n^{-*} (i.e., \mathbf{X}_n without the control parameter column). Then, we obtain tricands from \mathbf{X}_n^{-*} , which we will denote $\{\mathbf{X}_{\text{tri}} \mid \mathbf{X}_n^{-*}\}$. If there is a single nuisance parameter, the tricands are simply midpoints. Otherwise, they leverage the Delaunay triangulation discussed above. We then generate a one-dimensional grid of points, $\mathbf{x}_{\text{grid}}^*$, to span the full

support of the control parameter. Ultimately, we perform the Kronecker product between the grid and tricands to obtain the full d -dimensional candidate set, which we denote as $\mathbf{X}_{\text{tri}^+}$:

$$\mathbf{X}_{\text{tri}^+} := \mathbf{x}_{\text{grid}}^* \otimes \{\mathbf{X}_{\text{tri}} \mid \mathbf{X}_n^{-*}\}. \quad (6)$$

Figure 4 depicts this process visually. The left panel displays an initial LHS over the full d -dimensional space ($d = 3$ for this example). These training observations are then projected over the control parameter into $d - 1$ dimensions, creating \mathbf{X}_n^{-*} as illustrated by the gray lines and gray points in this figure. We generate tricands from the 2D \mathbf{X}_n^{-*} , denoted \mathbf{X}_{tri} (red stars in the center panel). Then, we create a semi-dense grid of 50 points for x^* . To offer a cleaner visual, Figure 4 shows only a 6-point $\mathbf{x}_{\text{grid}}^*$. We then perform the Kronecker product of \mathbf{X}_{tri} with $\mathbf{x}_{\text{grid}}^*$ to find $\mathbf{X}_{\text{tri}^+}$, as shown in the right panel.

While we designed this candidate set construction for estimation of $T(x^*)$, we find that it also works well as a discrete set of candidates for the next acquisition, \mathbf{x}_{n+1} . In our profile Bayesian optimization procedure, we will select subsequent acquisitions from our proposed $\mathbf{X}_{\text{tri}^+}$.

3.2 Acquisitions

Our modified tricands enable the use of PEI in higher dimensions, as they avoid the computational barrier of dense grids. But PEI as a sole acquisition metric will often cluster acquisitions near the global minima rather than acquiring points across the full support of x^* . To remedy this lack of exploration, we propose a new two-stage acquisition procedure that prioritizes exploration of \mathcal{X}^* while still leveraging the exploitative power of PEI. Our primary aim is to drive down uncertainty in our estimation of $T(x^*)$ while retaining accuracy, within the constraints of a limited training budget.

Given a surrogate f_n , trained on observations $\mathcal{D}_n = \{\mathbf{X}_n, \mathbf{y}_n\}$, we seek to acquire $\mathbf{x}_{n+1} = \{x_{n+1}^*, \mathbf{x}_{n+1}^{-*}\}$ to maximize learning of $T(x^*)$ (Eq. 1). We first generate $\mathbf{X}_{\text{tri}^+}$ following Eq. (6), but with one modification. Since we are going to repeat this procedure multiple times (until our training budget is exhausted), we replace the fixed evenly-spaced grid $\mathbf{x}_{\text{grid}}^*$, which would remain constant throughout the entire optimization, with a 1D LHS $\mathbf{x}_{\text{LHS}}^*$, which is re-randomized for each iteration. The LHS in 1D offers effective coverage of \mathcal{X}^* , while providing variability in the exact x^* values that are considered. We then estimate $\hat{T}(x^*)$ using these candidates as described in Section 2.1. Let $\text{CI}_T^{\text{wd}}(x^*)$ represent the width between the 97.5% and 2.5% quantiles for a particular x^* , which serves as a measure of uncertainty in our estimate. For our next acquisition, we select the x^* value with the largest uncertainty:

$$x_{n+1}^* = \underset{x^* \in \mathbf{x}_{\text{LHS}}^*}{\text{argmax}} \text{CI}_T^{\text{wd}}(x^*). \quad (7)$$

Then, we select \mathbf{x}_{n+1}^{-*} by maximizing PEI along the chosen slice:

$$\mathbf{x}_{n+1}^{-*} = \underset{\mathbf{x}^{-*} \in \{\mathbf{X}_{\text{tri}} \mid \mathbf{X}_n^{-*}\}}{\text{argmax}} \text{PEI}(\mathbf{x} = [x_{n+1}^*, \mathbf{x}^{-*}] \mid \mathcal{D}_n). \quad (8)$$

This calculation is very easy since our tricands set is not too large and $\mu_T(x_{n+1}^*)$ has already been estimated. We then observe $y_{n+1} = f(\mathbf{x}_{n+1})$, update our surrogate, and repeat until our evaluation budget has been spent. Our complete PBO procedure is outlined in Algorithm 1. Notice, although we use a 1D LHS through the acquisition loop, we prefer to use an evenly spaced grid in our final estimation.

Algorithm 1: Profile Bayesian Optimization.

Inputs: Black-box simulator f , initial training data $\{\mathbf{X}_n, \mathbf{y}_n\}$, trained surrogate f_n , maximum number of simulator evaluations m

for $i = (n + 1), \dots, m$ **do**

 Generate $\mathbf{X}_{\text{tri}^+} = \mathbf{x}_{\text{LHS}}^* \otimes \{\mathbf{X}_{\text{tri}} \mid \mathbf{X}_n^{-*}\}$

 Estimate $\hat{T}(x^*)$

 Select x_{n+1}^* with largest uncertainty (Eq. 7)

 Select \mathbf{x}_{n+1}^{-*} by maximizing PEI (Eq. 8)

 Update $\mathbf{X}_n = \{\mathbf{X}_n, \mathbf{x}_{n+1}\}$ and $\mathbf{y}_n = \{\mathbf{y}_n, f(\mathbf{x}_{n+1})\}$

 Retrain surrogate

 Increment $n = n + 1$

Output: Final $\hat{T}(x^*)$ using $\mathbf{X}_{\text{tri}^+} = \mathbf{x}_{\text{grid}}^* \otimes \{\mathbf{X}_{\text{tri}} \mid \mathbf{X}_n^{-*}\}$

Figure 5 offers an inside look at this process for the Branin function. Starting with $\hat{T}(x^*)$ estimated from our 10-point LHS (left panel here, also shown earlier in Figure 2), we select the x^* with the widest $\text{CI}_T(x^*)$, marked here by the blue dotted line. Then we choose the tricards point in the nuisance parameter space with the largest PEI on that slice. The center and right panels show progress after 10 and 20 PBO acquisitions, respectively. As the design progresses, our estimation of $T(x^*)$ exhibits increased accuracy and decreased uncertainty. The gray circles indicate data points that were selected by our PBO procedure (some of them are cut-off above, having $y > 20$). Many of the acquired points fall near the true minimum of their respective slice, indicating that PEI is effectively exploiting the minimum on the selected slices.

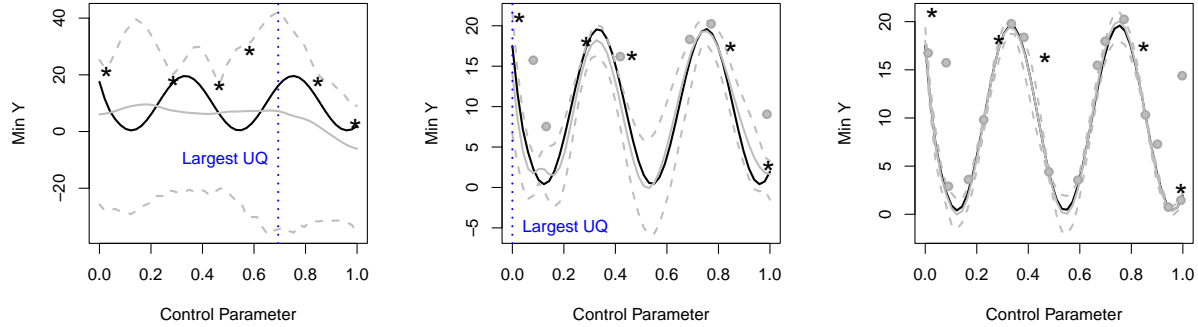


Figure 5: $\hat{T}(x^*)$ (solid/dashed gray) for the Branin function from an initial 10-point LHS (left), followed by 10 PBO acquisitions (center), and another 10 PBO acquisitions (right). Black lines mark the true $T(x^*)$. Blue dotted lines mark the x^* values with the widest uncertainty. Black stars and gray circles represent observations from the initial LHS and PBO acquisitions, respectively.

4 Synthetic Examples

In this section, we validate the performance of our proposed PBO against state-of-the-art alternatives on a variety of benchmark exercises. We measure performance of the estimation of $T(x^*)$ in four ways. First, to compare accuracy we assess average performance with root mean squared prediction error (RMSE, lower is better) and worst-case performance with maximum absolute deviation (MaxAD, lower is better). Then, to understand the quality of our uncertainty quantification, we consider both the coverage and the average

width of the 95% credible intervals (the latter is denoted AvgCI). Narrower CIs are preferred as long as the coverage is high, preferably near 95%. Formal definitions of all metrics are provided in Supplement A.

In the following sections, we will consider stationary and nonstationary examples, demonstrating applicability to both GP and DGP surrogates. For all surrogates, we use a fixed nugget of 1.0×10^{-6} to reflect the deterministic nature of the functions. Training budgets are adjusted based on the dimension and complexity of each test function. We prescale inputs to $\mathcal{X} = [0, 1]^d$ and responses to have zero mean and unit variance. For all methods, we use our modified tricands with 1,000 posterior samples to estimate $\hat{T}(x^*)$. All exercises are repeated with 30 re-randomized starting designs. Reproducible code for all synthetic experiments is available in our public repository.¹

4.1 Stationary Functions

For our stationary examples, we fit GP surrogates with separable lengthscales and Matérn kernels using the “scaled Vecchia” implementation of [Katzfuss et al. \(2022\)](#), which is built upon the `GpGp` ([Guinness et al., 2024](#)) and `GPvecchia` ([Katzfuss et al., 2024](#)) R packages. We do not need Vecchia approximation for training purposes given our small data sizes, but we do use Vecchia approximation for fast joint posterior sampling. Throughout, we use a conditioning set size of 40 when drawing Vecchia-approximated samples.

We compare our PBO procedure to a random LHS of equivalent size, a typical Bayesian optimization using multi-start gradient-based maximization of expected improvement, and the PEI approach of [Ginsbourger et al. \(2014\)](#). The LHS serves as a baseline only—its design is not sequential, and it does not use surrogates to select design locations. The typical BO serves as a different benchmark, showing the consequences of targeting global optima over profile optima. To enable the use of PEI as a comparator in higher dimensions, we also use our modified tricands as potential PEI acquisitions.

First, we revisit the 2D Branin function shown earlier in Figure 1, starting with a random LHS of size $n = 10$ and ending with a total budget of $m = 30$. Figure 5 showed the resulting $\hat{T}(x^*)$ from one repetition of our PBO procedure. Similar figures for the LHS, BO, and PEI methods are provided in Supplement C.

Figure 6 shows the performance across 30 re-randomized starting designs. All methods achieved adequate coverage of the true $T(x^*)$, slightly above 95%. The LHS benchmark has the largest error (RMSE/MaxAD) and the widest uncertainty intervals (AvgCI). This is to be expected as the LHS design makes no attempt to target minima. BO offers significant improvement, aided by the fact that this function has three global optima, but still tends to have large uncertainty. PEI and PBO performed equally well, offering the lowest error metrics with the tightest UQ.

¹<https://bitbucket.org/boothlab/rdc/>

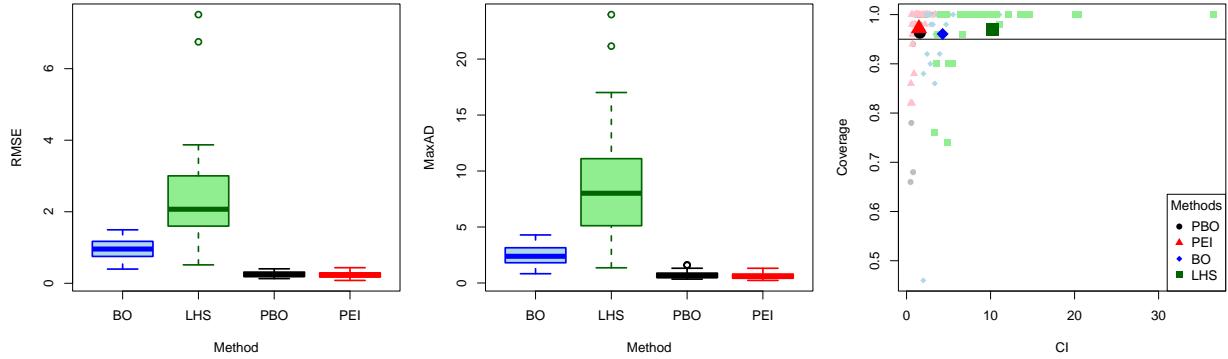


Figure 6: Results for the Branin function across 30 repetitions with $n = 10$ and $m = 30$. Large colored symbols in the right panel represent mean performance.

Our second stationary example is the 3D “Kyger3D” function, defined in [Supplement A](#). We begin with $n = 15$ and end with $m = 35$. Results are shown in [Figure 7](#). Unsurprisingly, LHS and BO struggle to estimate the profile optima, but this time PEI performs just as poorly. BO and PEI have narrower uncertainty intervals than LHS, but at the cost of sufficient coverage. To explain PEI’s poor performance, [Figure 8](#) shows an estimated $\hat{T}(x^*)$ from a single starting design for both PBO and PEI. PBO provides an effective estimate of the true $T(x^*)$ (shown in black) with high accuracy and tight uncertainty across the full control parameter range. In contrast, PEI overfocuses on the global minimum, spending half of its budget in this area. The lack of exploration over the control parameter leads to poor estimation of profile optima that are not near the global optima. PEI favors exploitation over exploration, leading to these clustered acquisitions. PBO performs better because its two-stage “explore then exploit” acquisition procedure strikes an effective balance.

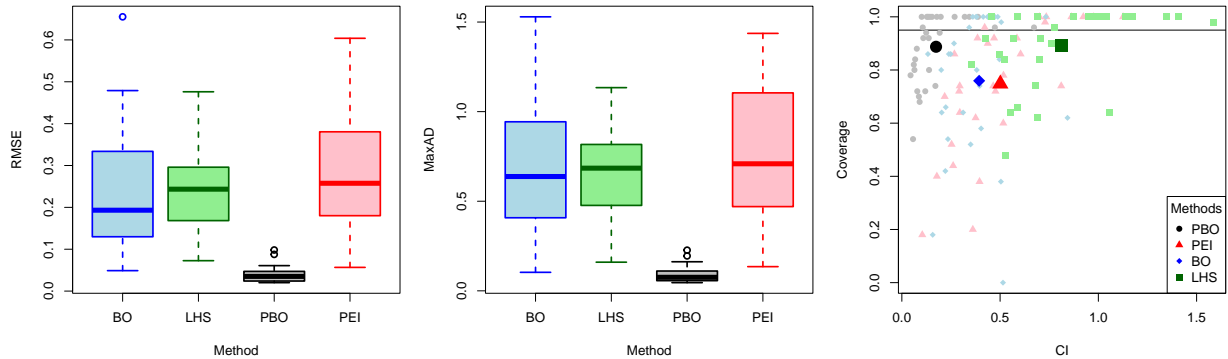


Figure 7: Results for the Kyger3D function across 30 repetitions with $n = 15$ and $m = 35$.

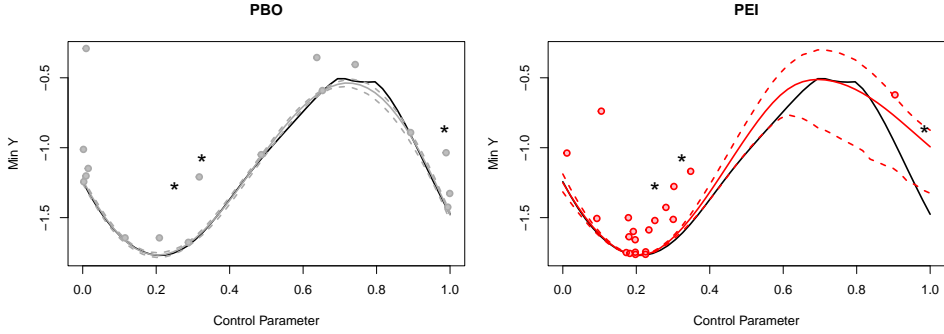


Figure 8: PBO and PEI estimation of $T(x^*)$ for the Kyger3D function. Black stars indicate initial LHS points, and colored circles indicate acquired points. The solid black line denotes the true $T(x^*)$, the solid colored lines denote $\mu_T(x^*)$, and the dashed colored lines denote $CI_T(x^*)$.

4.2 Nonstationary Functions

For our nonstationary examples, we use the `deepgp` R package (Booth, 2025b) to fit two-layer DGPs with Matérn kernels. We conduct 10,000 MCMC iterations for initial fits and 2,000 for subsequent fits after each new acquisition (initializing $\mathbf{W}_n^{(0)}$ and all hyperparameters with the last sampled values from the previous fit). We also set $\mu_w = \mathbf{X}$ (Eq. 3). We remove half of the MCMC iterations for burn-in, then thin down to 100 iterations. Joint posterior samples are generated from the modified tricards set with 10 samples coming from each MCMC iteration, for a total of 1,000. To provide insight into the benefit of the DGP’s flexibility, we compare our PBO procedure with a stationary GP against the same procedure with the nonstationary DGP. We drop BO and PEI as competitors given their poor performance in Section 4.1, but we retain the LHS benchmark, using both GP and DGP surrogates on the same LHS designs.

Our first nonstationary example is the 2D “Kyer2D” function defined in Supplement A. We consider this function weakly nonstationary. We begin with $n = 20$ and end with $m = 40$. Figure 9 shows the true $T(x^*)$ (black) with resulting estimates from LHS and PBO designs using both GP and DGP surrogates. Figure 10 shows performance across all 30 seeds. Although all LHS designs struggle to identify $T(x^*)$, those using DGP surrogates have much better performance than those using GPs. The LHS GP performs worse in RMSE and MaxAD and has consistently wider uncertainty than its DGP counterpart. The performance differences between the PBO GP and PBO DGP designs are less stark, although the DGP does offer better worst-case performance in RMSE and MaxAD; both suffer from a degree of overconfidence. Interestingly, improved accuracy is often accompanied by decreased coverage—we will discuss this and potential remedies in Section 6. Overall, the use of the strategic PBO design over the static LHS proved more impactful than the choice of surrogate.

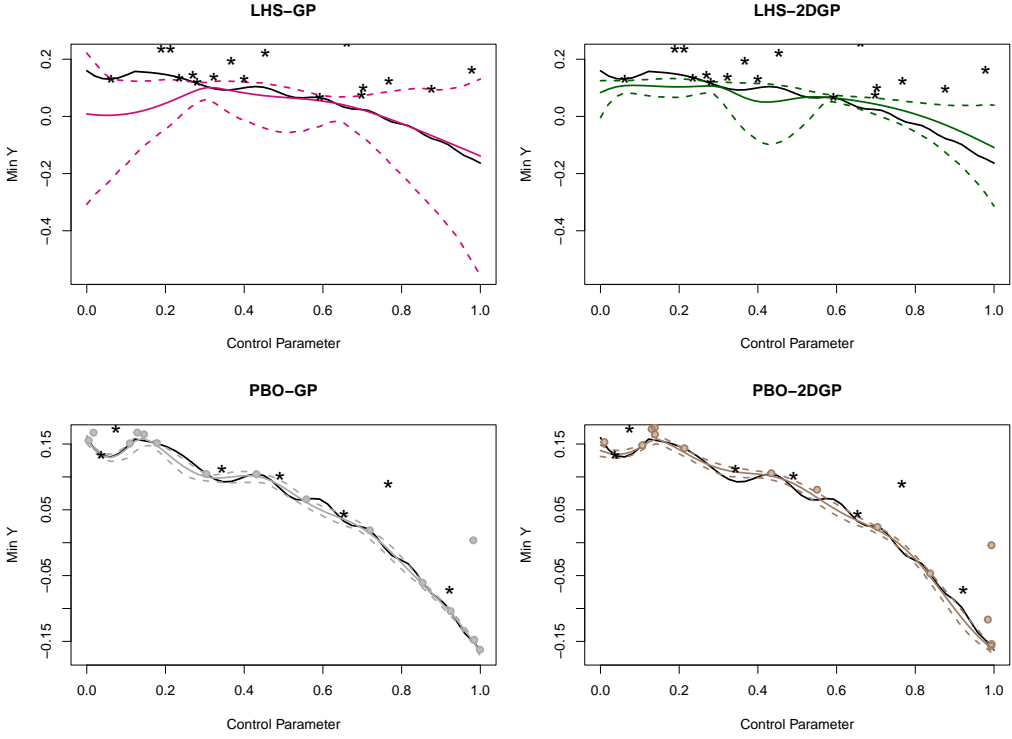


Figure 9: Estimation of $T(x^*)$ for the Kyger2D function using GP/DGP surrogates with LHS and PBO.

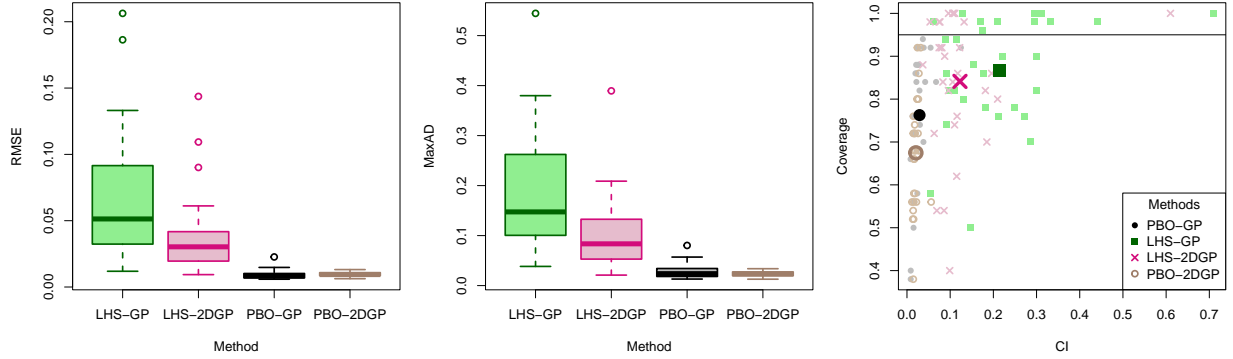


Figure 10: Results for the Kyger2D function across 30 repetitions with $n = 20$ and $m = 40$.

The second nonstationary example is the ‘‘squiggle’’ function (Rumsey, 2025; Rumsey et al., 2025), which we have adapted from its original 2D form to create a similar 4D function (Supplement A). The squiggle function exhibits more nonstationarity than the Kyger2D function. We begin with $n = 40$ and end with $m = 80$, with results presented in Figure 11. Again, we see better performance from the LHS DGP than the LHS GP, with consistently lower RMSE/MaxAD and comparable UQ. We suspect the starker improvements of the DGP over the GP are owed to the increased dimensionality and complexity of the function. Both PBO designs outperform their LHS counterparts, with significantly better accuracy and improved UQ. The PBO DGP offered the best performance, although it again tended to be overconfident in its predictions.

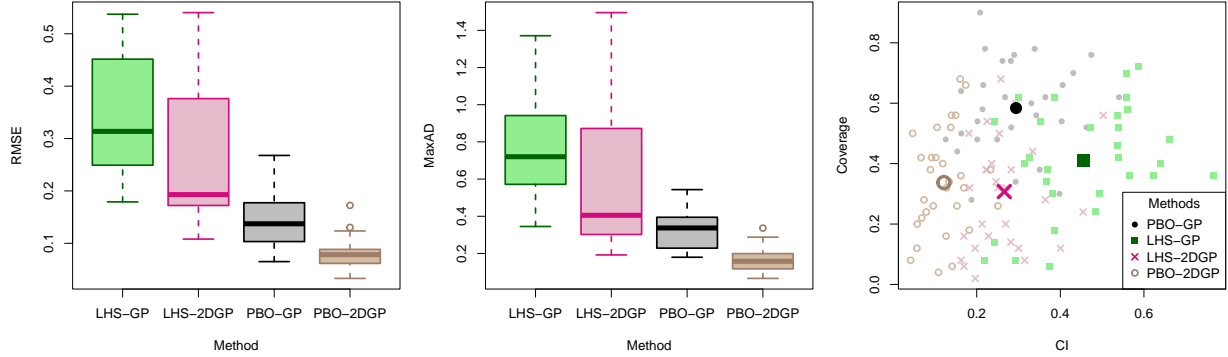


Figure 11: Results for the squiggle function across 30 repetitions with $n = 40$ and $m = 80$.

5 RDC-Diffuser

Rotating detonation combustors utilize a circumferentially rotating detonation wave to consume fuel and initiate combustion, as depicted in the left panel of Figure 12. RDCs may increase thermodynamic efficiency up to 20% when compared to standard conventional combustors, which could reduce fuel consumption within an engine by up to 9% with the same power output (Jones and Paxson, 2013). Power extraction requires the flow exiting a combustor to enter a gas turbine, but this process poses several challenges. Detonation combustion invokes high temperatures, presenting issues with thermal management (Heiser and Pratt, 2002). The rotating detonation wave travels along the walls of the combustor at high speeds, resulting in high frequency pulses and permeations within the flow which can inhibit power extraction (Fernelius et al., 2013). Also, the flow speed must be reduced to appropriate levels for the provided turbine.

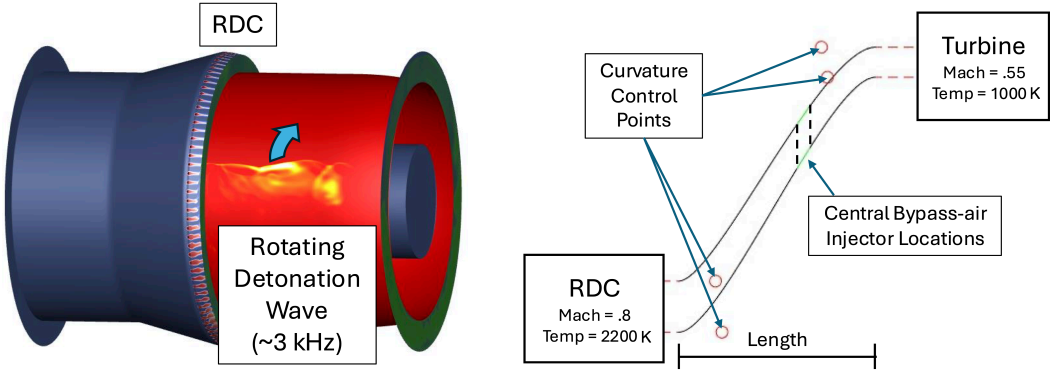


Figure 12: *Left:* Schematic of a detonation wave traveling through an RDC. *Right:* Parameterized geometry for a 2D slice of the diffuser. Flow speed and temperature are reduced upon exiting the diffuser.

The diffuser, which will mix the hot exhaust and cold bypass-air downstream of the RDC, is designed to condition and cool the flow and reduce negative oscillatory effects from the rotating detonation wave. Diffusers hold great potential to improve the efficiency of power extraction from RDCs. Naples et al. (2014) replaced the stock combustor of a T63 helicopter engine with an RDC-diffuser and found that oscillations were damped by 60-70% and hot exhaust temperatures were reduced to near ideal levels. Grunenwald

(2023) explored the integration of an RDC-diffuser into a Rolls Royce M250 engine and found that non-axial flows could be forced into a more linear regime through a “swan-neck” shaped diffuser, resulting in a more uniform flow.

While diffusers show great promise, the potential for them to improve RDC power efficiency is contingent on effective design. Here, we work with a computer simulation that returns the pressure lost through diffusion as a function of 6 design parameters: length, location of cold bypass-air inlets, and 4 control points that determine the curvature. The right panel of Figure 12 offers a simple representation of the diffuser and its parameterization. To demonstrate the significance of the diffuser’s length on energy efficiency, Figure 13 depicts two 2D diffusers of varying lengths, but with identical normalized curvatures. The short diffuser has a large pressure loss of 26.43%, indicating poor energy efficiency. The longer diffuser has a low pressure loss of 9.2%, but the temperatures of the flow at the walls exceeds 1000K, which could cause the diffuser to melt.

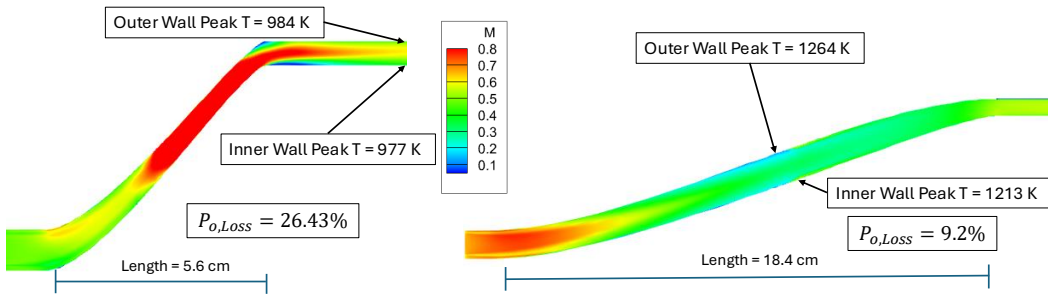


Figure 13: Pressure loss (P) with Mach number (M) and temperature (T) for two runs of the 6D diffuser simulation with a short length (left) and a long length (right).

We implement our PBO procedure to identify the profile optima in pressure loss as a function of the diffuser’s length (leaving 5 nuisance parameters). The complex dynamics of the RDC-diffuser power output warrant the nonstationarity of a DGP surrogate. Figure 14 displays $\hat{T}(x^*)$ as our PBO procedure progresses. We begin with a 50-point 6D LHS (left panel), with observed points marked by black stars. The lowest pressure points are visible; observations with higher pressures are cut off above. Then, we fit a two-layer DGP, as described in the beginning of Section 4.2. The resulting estimate for $T(x^*)$ is displayed with a black line denoting $\mu_T(x^*)$ and dashed gray lines denoting $CI_T(x^*)$. The UQ is large for this initial estimation, which is to be expected given the input dimension ($d = 6$) and limited sample size ($n = 50$).

The center panel shows the updated $\hat{T}(x^*)$ after fifty PBO acquisitions (gray circles). $CI_T(x^*)$ has narrowed significantly across the full support of the control parameter, but the surrogate still sees potential for improvement, with many of the CI intervals living well below observed data points. This motivated an additional fifty acquisitions, for a total of $m = 150$. The right panel shows this final estimation of $T(x^*)$. The mean prediction is barely changed, but the uncertainty has shrunk considerably, with the majority of our acquisitions lying on or near $\mu_T(x^*)$. Although we do not know the truth, we take this as a good indication that our procedure is providing effective and reliable estimates.

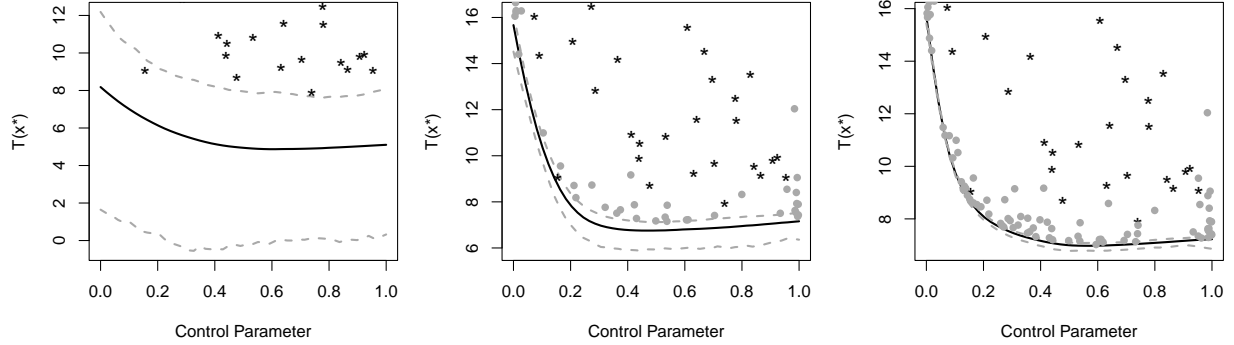


Figure 14: Diffuser results from an original 50-point LHS (left), after 50 acquisitions (center), and after 100 acquisitions (right). Solid black line denotes $\mu_T(x^*)$, and dashed gray lines denote $CI_T(x^*)$. Black stars indicate initial LHS points; gray circles indicate PBO acquisitions.

6 Conclusion

Our aim was to identify the profile optima (Eq. 1) of a deterministic black-box computer simulation over the full support of a single control parameter ($x^* \in \mathcal{X}^*$) given a limited evaluation budget. Traditional Bayesian optimization is not designed to explore the full control parameter space, making it ill-equipped for profile optimization. Prior work on profile optimization was limited to two-dimensional functions and similarly tended to over-exploit near global optima. We proposed a novel two-stage surrogate-informed acquisition method, termed profile Bayesian optimization. The first step forces exploration of \mathcal{X}^* by identifying the x^* with the largest uncertainty in the surrogate’s estimation of $T(x^*)$. The second step selects nuisance parameter values by maximizing profile expected improvement along the chosen slice. Our two-stage approach is feasible in higher dimensions and is compatible with nonstationary DGP surrogates, which can provide superior predictions of complex functions. Our procedure performed favorably on various synthetic examples, improving upon space-filling designs as well as existing BO and profile optimization methods. On our motivating computer experiment, our procedure provided a useful estimate of the profile optima from only 150 simulator evaluations.

There are several interesting avenues for future research in this area. Our methodology is designed for functions that have a unique profile optimum for each x^* . Functions with non-unique profile optima will likely warrant adaptations to our current methodology; we leave this as an avenue for future work. There is also potential to improve our modified tricands procedure, particularly in the allocation of fringe candidates. In our tests, we set fringe candidates to be placed at 90% of the distance to the boundary. This gets close to corners and borders, but it avoids placing candidates squarely on the boundary. If the profile optima is found in a corner, our candidates could struggle to find them quickly. Additionally, as input dimension increases (beyond what we considered here), tricands may become computationally infeasible and suboptimal in their coverage. In these cases, adaptations like Voronoi candidates (Wycoff et al., 2025) may be necessary.

In our nonstationary test functions, we noticed an interesting phenomenon: our more flexible DGP surrogates, although offering the best accuracy, suffered from low coverage. This is worthy of investigation; perhaps there are better ways to estimate uncertainty in $\hat{T}(x^*)$. Our approach, based on the empirical distribution of minimums obtained from joint posterior samples, is contingent upon having a sufficient number of posterior samples to adequately cover the tails of the posterior. Increasing the number of posterior samples from the 1,000 that we used may improve the uncertainty estimates. We suspect this

trend appeared with the DGP surrogates since more flexible models are likely to have “peakier” optima that might be missed with smaller sample sizes.

There are many avenues for extensions in our motivating application. To improve surrogates of our RDC-diffuser simulation, we will explore gradient-enhancement, which can offer huge improvements in surrogate performance from the same budget of simulator evaluations. This will involve upgrading our simulation to return gradients through the use of adjoint solvers, then employing gradient-enhanced DGP surrogates (Booth, 2025a). Extensions of our PBO procedure that incorporate temperature constraints would be relevant, as excessive temperatures put the diffuser in danger of melting. We also plan to leverage Bayesian calibration (Kennedy and O’Hagan, 2001) to calibrate our computer experiment with data from physical lab experiments, where noise and bias may be present. Ultimately, our RDC-diffuser simulation has potential to serve as a digital twin (Willcox et al., 2023) of a real RDC-diffuser in an engine.

Acknowledgements

This work was supported by the U.S. National Science Foundation under Award Number 2533443.

References

Berk, J., Nguyen, V., Gupta, S., Rana, S., and Venkatesh, S. (2018). “Exploration enhanced expected improvement for Bayesian optimization.” In *joint european conference on machine learning and knowledge discovery in databases*, 621–637. Springer.

Booth, A. S. (2025a). “Deep Gaussian Processes with Gradients.” *arXiv preprint arXiv:2512.18066*.

— (2025b). *deepgp: Bayesian Deep Gaussian Processes using MCMC*. R package version 1.2.0.

Booth, A. S., Cooper, A., and Gramacy, R. B. (2024). “Nonstationary Gaussian process surrogates.” *arXiv preprint arXiv:2305.19242*.

Booth, A. S., Renganathan, S. A., and Gramacy, R. B. (2025). “Contour location for reliability in airfoil simulation experiments using deep gaussian processes.” *The Annals of Applied Statistics*, 19, 1, 191–211.

Chen, Z., Mak, S., and Wu, C. J. (2024). “A hierarchical expected improvement method for Bayesian optimization.” *Journal of the American Statistical Association*, 119, 546, 1619–1632.

Damianou, A. and Lawrence, N. D. (2013). “Deep Gaussian processes.” In *Artificial intelligence and statistics*, 207–215. PMLR.

Fernelius, M., Gorrell, S. E., Hoke, J., and Schauer, F. (2013). “Effect of periodic pressure pulses on axial turbine performance.” In *49th AIAA/ASME/SAE/ASEE Joint Propulsion Conference*, 3687.

Frazier, P. I. (2018). “Bayesian optimization.” In *Recent advances in optimization and modeling of contemporary problems*, 255–278. Informs.

Ginsbourger, D., Baccou, J., Chevalier, C., Perales, F., Garland, N., and Monerie, Y. (2014). “Bayesian Adaptive Reconstruction of Profile Optima and Optimizers.” *SIAM/ASA Journal on Uncertainty Quantification*, 2, 1, 490–510.

Gramacy, R. B. (2020). *Surrogates: Gaussian Process Modeling, Design and Optimization for the Applied Sciences*. Boca Raton, Florida: Chapman Hall/CRC. <http://bobby.gramacy.com/surrogates/>.

Gramacy, R. B., Sauer, A., and Wycoff, N. (2022). “Triangulation candidates for Bayesian optimization.” *Advances in Neural Information Processing Systems*, 35, 35933–35945.

Grunenwald, J. (2023). “Investigation of Rotating Detonation Physics and Design of a Mixer for a Rotating Detonation Engine.” Master’s thesis, Purdue University.

Guinness, J., Katzfuss, M., and Fahmy, Y. (2024). *GpGp: Fast Gaussian Process Computation Using Vecchia’s Approximation*. R package version 0.5.1.

Heiser, W. H. and Pratt, D. T. (2002). “Thermodynamic cycle analysis of pulse detonation engines.” *Journal of propulsion and power*, 18, 1, 68–76.

Jones, D. R., Schonlau, M., and Welch, W. J. (1998). “Efficient global optimization of expensive black-box functions.” *Journal of Global optimization*, 13, 4, 455–492.

Jones, S. M. and Paxson, D. E. (2013). “Potential benefits to commercial propulsion systems from pressure gain combustion.” In *49th AIAA/ASME/SAE/ASEE Joint Propulsion Conference*, 3623.

Katzfuss, M. and Guinness, J. (2021). “A general framework for Vecchia approximations of Gaussian processes.” *Statistical Science*, 36, 1, 124–141.

Katzfuss, M., Guinness, J., Gong, W., and Zilber, D. (2020). “Vecchia approximations of Gaussian-process predictions.” *Journal of Agricultural, Biological and Environmental Statistics*, 25, 3, 383–414.

Katzfuss, M., Guinness, J., and Lawrence, E. (2022). “Scaled Vecchia approximation for fast computer-model emulation.” *SIAM/ASA Journal on Uncertainty Quantification*, 10, 2, 537–554.

Katzfuss, M., Jurek, M., Zilber, D., and Gong, W. (2024). *GPvecchia: Scalable Gaussian-Process Approximations*. R package version 0.1.7.

Kennedy, M. C. and O’Hagan, A. (2001). “Bayesian calibration of computer models.” *Journal of the Royal Statistical Society: Series B (Statistical Methodology)*, 63, 3, 425–464.

Marmin, S. and Filippone, M. (2022). “Deep Gaussian processes for calibration of computer models (with discussion).” *Bayesian Analysis*, 17, 4, 1301–1350.

McKay, M. D., Beckman, R. J., and Conover, W. J. (2000). “A comparison of three methods for selecting values of input variables in the analysis of output from a computer code.” *Technometrics*, 42, 1, 55–61.

Ming, D., Williamson, D., and Guillas, S. (2023). “Deep Gaussian process emulation using stochastic imputation.” *Technometrics*, 65, 2, 150–161.

Murray, I., Adams, R., and MacKay, D. (2010). “Elliptical slice sampling.” In *Proceedings of the thirteenth international conference on artificial intelligence and statistics*, 541–548. JMLR Workshop and Conference Proceedings.

Naples, A., Hoke, J., and Schauer, F. (2014). “Rotating detonation engine interaction with an annular ejector.” In *52nd aerospace sciences meeting*, 0287.

Pourmohamad, T. and Lee, H. K. (2021). *Bayesian optimization with application to computer experiments*. Springer.

Qin, C., Klabjan, D., and Russo, D. (2017). “Improving the expected improvement algorithm.” *Advances in Neural Information Processing Systems*, 30.

Rajaram, D., Puranik, T. G., Ashwin Renganathan, S., Sung, W., Fischer, O. P., Mavris, D. N., and Ramamurthy, A. (2021). “Empirical assessment of deep gaussian process surrogate models for engineering problems.” *Journal of Aircraft*, 58, 1, 182–196.

Rasmussen, C. E. and Williams, C. K. (2006). *Gaussian processes for machine learning*, vol. 2. MIT press.

Rumsey, K. (2025). *duqling: Library of UQ Test Functions*. R package version 2.0.0, commit b5df65ce6691434919e00b28455bea08f64abbe7.

Rumsey, K. N., Gibson, G. C., Francom, D., and Morris, R. (2025). “All Emulators are Wrong, Many are Useful, and Some are More Useful Than Others: A Reproducible Comparison of Computer Model Surrogates.” *arXiv preprint arXiv:2512.09060*.

Sampson, P. D. and Guttorp, P. (1992). “Nonparametric estimation of nonstationary spatial covariance structure.” *Journal of the American Statistical Association*, 87, 417, 108–119.

Santner, T. J., Williams, B. J., Notz, W. I., and Williams, B. J. (2003). *The design and analysis of computer experiments*, vol. 1. Springer.

Sauer, A., Cooper, A., and Gramacy, R. B. (2023a). “Non-stationary Gaussian process surrogates.” *arXiv preprint arXiv:2305.19242*.

— (2023b). “Vecchia-approximated deep Gaussian processes for computer experiments.” *Journal of Computational and Graphical Statistics*, 32, 3, 824–837.

Sauer, A., Gramacy, R. B., and Higdon, D. (2023c). “Active learning for deep Gaussian process surrogates.” *Technometrics*, 65, 1, 4–18.

Sauer, A. E. (2023). “Deep Gaussian process surrogates for computer experiments.” Ph.D. thesis, Virginia Tech.

Schmidt, A. M. and O’Hagan, A. (2003). “Bayesian inference for non-stationary spatial covariance structure via spatial deformations.” *Journal of the Royal Statistical Society Series B: Statistical Methodology*, 65, 3, 743–758.

Surjanovic, S. and Bingham, D. (2013). “Virtual Library of Simulation Experiments.” <https://www.sfu.ca/~ssurjano/index.html>.

Thompson, W. R. (1933). “On the likelihood that one unknown probability exceeds another in view of the evidence of two samples.” *Biometrika*, 25, 3/4, 285–294.

Vecchia, A. V. (1988). “Estimation and model identification for continuous spatial processes.” *Journal of the Royal Statistical Society Series B: Statistical Methodology*, 50, 2, 297–312.

Wang, X., Jin, Y., Schmitt, S., and Olhofer, M. (2023). “Recent advances in Bayesian optimization.” *ACM Computing Surveys*, 55, 13s, 1–36.

Willcox, K., Bingham, D., Chung, C., Chung, J., Cruz-Neira, C., Grant, C., Kinter, J., Leung, R., Moin, P., Ohno-Machado, L., et al. (2023). *Foundational research gaps and future directions for digital twins*. National Academies Press Washington, DC, USA.

Wycoff, N., Smith, J. W., Booth, A. S., and Gramacy, R. B. (2025). “Voronoi candidates for Bayesian optimization.” *Journal of Global Optimization*, 1–27.

Yazdi, F., Bingham, D., and Williamson, D. (2024). “Deep Gaussian Process Emulation and Uncertainty Quantification for Large Computer Experiments.” *arXiv preprint arXiv:2411.14690*.

Zhan, D. and Xing, H. (2020). “Expected improvement for expensive optimization: a review.” *Journal of Global Optimization*, 78, 3, 507–544.

SUPPLEMENTARY MATERIAL

A Test Functions

In this section we provide the formulaic details for the test functions used in Section 4. For all functions, we prescale inputs to $[0, 1]^d$ and responses to zero mean with unit variance before modeling.

The Branin function (Surjanovic and Bingham, 2013) is defined as

$$f(\mathbf{x}) = a \left(x_2 - bx_1^2 + c_x 1 - r \right)^2 + s (1 - t) \cos(x_1) + s \quad \text{for } x_1 \in [-5, 10] \quad x_2 \in [0, 15].$$

The (stationary) Kyger3D function is defined as:

$$f(\mathbf{x}) = \exp(-x_1 - \cos(2\pi x_1)) + \sin(2\pi x_3) + \exp(-x_3 * \sin(2\pi x_1)) + \cos(2\pi x_2) - \exp(-x_2 * \cos(2\pi x_1)) \quad \text{for } x_1, x_2 \in [0, 1].$$

The (nonstationary) Kyger2D function is defined as:

$$f(\mathbf{x}) = \left(\sin(x_1^2) + 1 + \sum_{i=1}^2 (x_i - 0.5)^2 \right) (\cos(x_2) + 1.5) \left(e^{\{4 - \frac{x_1}{3}\}} \right) - (x_1 - 0.1) \sum_{i=1}^2 (x_i^2) \quad \text{for } x_1 \in [0, 2\pi] \quad x_2 \in [0, 5\pi/2].$$

The Squiggle function (Rumsey, 2025; Rumsey et al., 2025) is defined as:

$$f(\mathbf{x}) = x_1 \phi \left(\frac{\sum_{i=2}^4 x_i^2 - [\sin(2\pi x_1^2) / 4 - x_1 / 10 + 0.5]}{\sigma} \right) \quad \text{for } x_1, x_2, x_3, x_4 \in [0.1, 1], \quad \sigma = 0.2,$$

where ϕ is the standard Gaussian probability density function.

B Performance Metrics

Let $\mathbf{x}_{\text{grid}}^*$ represent an evenly spaced grid of size n_g covering the control parameter space \mathcal{X}^* . We obtain estimates of $T(x^*)$ at each $x^* \in \mathbf{x}_{\text{grid}}^*$ (Algorithm 1). Let $\mu_T(x^*)$ denote the mean and $\text{CI}_T(x^*)$ denote the 95% CI, with a width of $\text{CI}_T^{\text{wd}}(x^*)$. Our performance metrics are defined as follows:

$$\begin{aligned} \text{RMSE} &= \sqrt{\frac{1}{n_g} \sum_{x^* \in \mathbf{x}_{\text{grid}}^*} (\mu_T(x^*) - T(x^*))^2} \\ \text{MaxAD} &= \max_{x^* \in \mathbf{x}_{\text{grid}}^*} (|\mu_T(x^*) - T(x^*)|) \\ \text{AvgCI} &= \frac{1}{n_g} \sum_{x^* \in \mathbf{x}_{\text{grid}}^*} \text{CI}_T^{\text{wd}}(x^*) \\ \text{Coverage} &= \frac{1}{n_g} \sum_{x^* \in \mathbf{x}_{\text{grid}}^*} \mathbb{1}_{\{T(x^*) \in \text{CI}_T(x^*)\}} \end{aligned}$$

C Additional Results

Figure 15 shows estimated $\hat{T}(x^*)$ for all four comparators on the 2D Branin function exercise of Section 4.1. All methods start with the same initial LHS of size $n = 10$ and proceed with 20 acquisitions for a total of $m = 30$.

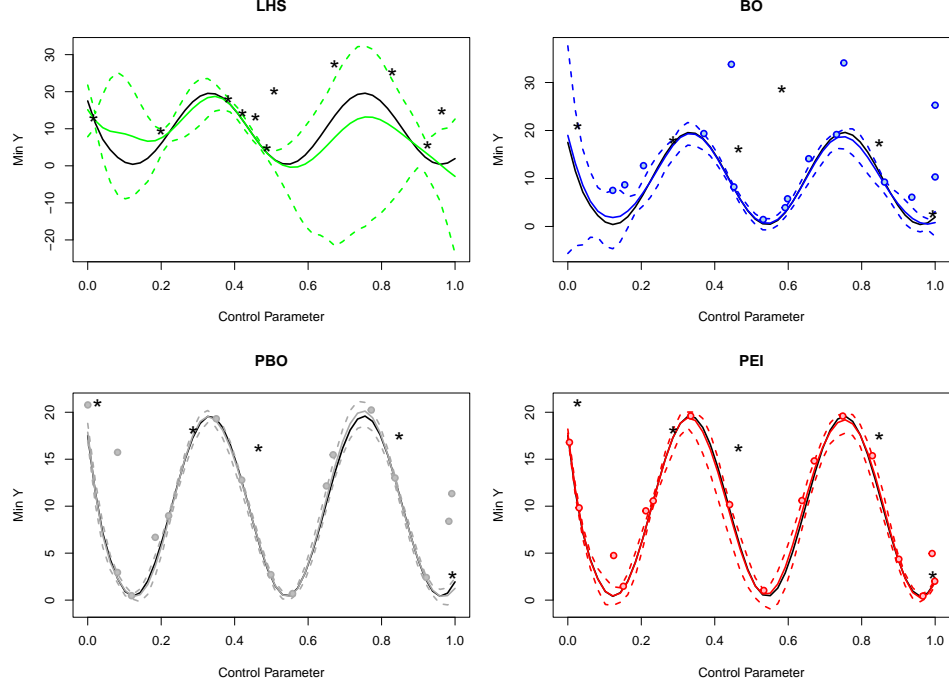


Figure 15: Estimation of $T(x^*)$ for the Branin Function. Truth in solid black. Colored solid/dashed lines denote $\mu_T(x^*)$ and $CI_T(x^*)$ for each method. Black stars indicate LHS observations; colored circles indicate acquired points.